

Novel metrics and application of nearest-neighbor feature selection for comparing resting-state fMRI brain atlases

Bryan A. Dawkins¹, Rayus Kuplicki², Trang T. Le³, Alejandro A. Hernandez¹,
and Brett A. McKinney^{1,4,*}

¹Department of Mathematics, University of Tulsa, Tulsa, OK 74104, USA

²Laureate Institute for Brain Research, Tulsa, OK 74136, USA

³Department of Biostatistics, Epidemiology and Informatics, University of
Pennsylvania, Philadelphia, PA 19104

⁴Tandy School of Computer Science, University of Tulsa, Tulsa, OK 74104, USA

*Correspondence: brett.mckinney@gmail.com

Abstract

Resting-state functional connectivity MRI (rs-fMRI) data consists of correlation matrices, where correlations are computed between the time series from brain Regions of Interest (ROIs). There are many different parcellations of the human brain into collections of ROIs. These parcellations, or atlases, can be used in case-control studies in order to understand and accurately classify subject phenotypes. We present new metrics for nearest-neighbor distance-based feature selection at the ROI level. Using our new metrics, we apply a novel nearest-neighbor feature selection algorithm to calculate relative importance of ROIs for classification of a binary outcome including major depression and healthy controls in two existing brain atlases. We use integer programming to derive a mapping between brain atlases to determine spatially similar ROIs. With ROI importance scores and spatial similarity between atlases, we present a novel modality for the comparison of brain atlases and the selection of ROIs relevant to major depression.

1 Background

Resting-state fMRI data exists in high dimensions and has many sources of noise, such as physiological or motion related [1]. Feature selection is typically done with the purpose of determining brain regions of interest (ROIs) that accurately discriminate between cases and controls in order to understand a particular phenotype. The data consists of pairwise ROI-ROI correlations, where each ROI is a time series measuring brain activity in a particular region or regions of the brain while a subject is not performing a task. A typical data set consists of m subject-specific correlation matrices of dimension $p \times p$, where the pairwise correlations are computed between p ROI time series with respect to a particular brain atlas.

Nearest-neighbor distance-based feature selection in rs-fMRI data has been performed using the private evaporative cooling method, which used pairwise ROI-ROI correlations as predictors of a particular phenotype [2]. However, nearest-neighbor feature selection algorithms have not been applied at the ROI level to assess the relative importance of ROIs for a given phenotype. To address this, we have previously proposed a new distance metric that allows us to compute the importance of individual ROIs using a nearest-neighbor distance-based approach [3]. We use this new distance metric with a novel nearest-neighbor feature selection algorithm called Nearest-neighbor Projected Distance Regression (NPDR) in order to compute ROI importance and the corresponding pseudo P values [4]. Our analysis is done on subject rs-fMRI correlation matrices generated

by two well known brain atlases with spherical [5] and anatomically shaped [6] ROIs, to which we refer as Power and Shen atlases, respectively. Cross sections through each atlas were visualized (Fig. 1) using the Analysis of Functional NeuroImages (AFNI) software [7].

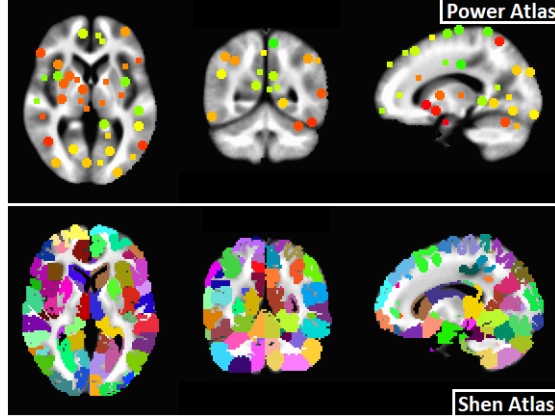


Fig 1. Two-dimensional slices through Power [5] and Shen [6] atlas ROIs. Slices are shown at the same locations in each atlas for the three different orientations. Atlases are in MNI space [8] so that voxel and ROI locations are comparable between them. Each atlas is labeled by the first author of the manuscripts in which they were introduced [5,6].

In order to make spatial comparisons between any pair of brain atlases, we first compute a distance matrix containing all pairwise distances between the different collections of atlas ROIs. Distances are defined based on a set dissimilarity metric that accounts for differences in voxel collections between pairs of ROIs. In a particular coordinate system, voxels have well defined three-dimensional locations in a given brain atlas. As long as two different atlases are in the same coordinate system, we can compare voxel membership between opposing atlas ROIs. We use an integer program that defines the standard Assignment Problem (AP) to find the one-to-one mapping between the two sets of atlas ROIs [9]. The collection of all mapped ROIs gives the closest spatial relationship between the two atlases. The collection of unmapped ROIs gives an indication of spatial uniqueness in the two atlases, respectively. All ROIs can be further mapped to a well defined anatomical region of the brain, which allows us to point out potential targets for better understanding the phenotype of interest.

Our spatial mapping between atlases and relative importance scores for ROIs in each respective atlas provides a way to combine relevant and distinct aspects of each brain atlas into a new parcellation. This new atlas could include important ROIs that are in the optimal one-to-one mapping from the solution to the assignment problem and any important unmapped ROIs from each atlas. Spatial overlap and attribute importance can serve as a useful tool for other researchers to compare, contrast, and combine two atlases. In particular, our results show how one might choose either of the two atlases to study the phenotype of interest we are considering in this work or a completely different phenotype.

2 Methods

In this section, we first describe real rs-fMRI data generated from healthy controls (HC) and subjects with major depressive disorder (MDD), where several of the MDD subjects also have an Anxiety Disorder (AD). Using integer programming, we then derive a one-to-one mapping between the ROIs in two brain atlases used to generate the real data mentioned previously. Finally, we use our new distance metric for rs-fMRI data, along with NPDR, to compute importance scores for ROIs in each atlas from the real data.

2.1 Real rs-fMRI data

Resting-state fMRI data was collected for a total of 59 healthy controls and 243 subjects with MDD. After filtering subjects based on head motion in the scanner, we have 40 healthy controls and 171 subjects with MDD. A total of 116 of the 171 MDD subjects also exhibit symptoms of an anxiety disorder, which leaves 55 that are without significant anxiety. For each subject, we generated a matrix of pairwise correlations between ROI time series. We used both the Power [5] and Shen [6] fMRI brain atlases, which consist of 277 and 278 ROIs, respectively.

2.2 Spatial overlap between brain atlases

Let R_A and R_B represent regions of interest (ROIs) in atlases A and B , respectively. We assume that atlases A and B are in the same coordinate space. Since R_A and R_B are just collections of voxels that have well defined three-dimensional coordinates, the spatial overlap between R_A and R_B can be defined as the set intersection between the two ROIs. Spatial dissimilarity between R_A and R_B can be computed with the Jaccard metric, which is given by the following

$$d^J(R_A, R_B) = \frac{|R_A \cup R_B - R_A \cap R_B|}{|R_A \cup R_B|}, \quad (1)$$

where the $(-)$ sign denotes set complement and $|\cdot|$ represents set cardinality. If the intersection $R_A \cap R_B$ is empty, then the two ROIs do not share any voxels and the Jaccard distance (Eq. 1) between them is 1. On the other hand, the Jaccard distance is 0 if the union $R_A \cup R_B$ and intersection $R_A \cap R_B$ are the same sets, which means the two ROIs have exactly the same voxels. All other possible Jaccard distances between R_A and R_B are strictly within $(0, 1)$. Hence, the Jaccard metric is contained within $[0, 1]$. The reason for division by $|R_A \cup R_B|$ in the denominator of the Jaccard metric (Eq. 1) is specifically to normalize the distance to be within $[0, 1]$. Otherwise, this distance between two ROIs would be affected by the cardinalities of R_A and R_B , respectively. The Jaccard metric is intuitive in this context because ROIs are not just points in space, but rather they can have irregular three-dimensional shapes. Therefore, a Euclidean metric that gives the straight-line distance between two points does not necessarily indicate ‘closeness’ between two ROIs. It is possible to compute the Euclidean distance between the centroids of two ROIs, but the ROIs may not share many voxels due to their potentially irregular shapes. Therefore, it is more informative to use a distance metric that uses set operations like the Jaccard metric (Eq. 1). We show an example (Fig. 2) of the Jaccard distance between ROIs R_A and R_B that contain n_1 and n_2 voxels, respectively.

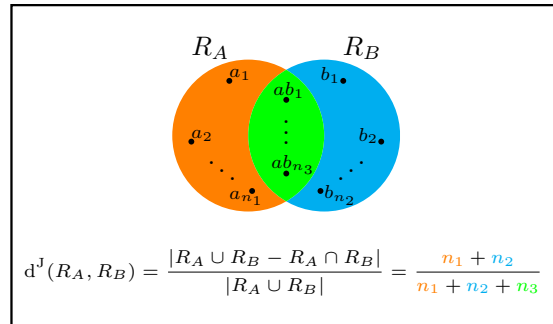


Fig 2. Example computation of Jaccard distance between ROIs R_A and R_B from two atlases A and B , respectively. There are n_1 , n_2 , n_3 voxels in R_A only, R_B only, and both R_A and R_B , respectively. The numerator gives the number of voxels unique to R_A (n_1) plus the number of voxels unique to R_B (n_2). The denominator contains the total number of voxels in R_A or R_B .

Each ROI in atlas A may overlap many different ROIs in atlas B . On the other hand, some ROIs in A may not overlap any ROIs in B . Furthermore, it is likely that A

and B contain different numbers of ROIs. If we want to compute a minimum distance one-to-one mapping between the atlases, it is possible that some ROIs in A will not have a mapped partner in B . In order to efficiently compute this atlas-atlas mapping, we formulate this task as a standard Assignment Problem [9], which has a very concise definition (Fig. 3).

$$\begin{array}{ll}
 \text{Min} & \sum_{i=1}^M \sum_{j=1}^N d_{ij} y_{ij} \\
 \text{s.t.} & \left. \begin{array}{l} \sum_{i=1}^M y_{i1} = 1 \\ \vdots \\ \sum_{i=1}^M y_{iN} = 1 \end{array} \right\} \text{Column Constraints} \\
 & \left. \begin{array}{l} \sum_{j=1}^N y_{1j} = 1 \\ \vdots \\ \sum_{j=1}^N y_{Mj} = 1 \end{array} \right\} \text{Row Constraints} \\
 & y_{ij} \in \{0, 1\} \quad \forall i, j
 \end{array}$$

Fig 3. Assignment problem mathematical definition. The assignment matrix Y is binary, where $y_{ij} = 0$ if nodes i and j are assigned to each other and 0 otherwise. The distance matrix D between all nodes is computed to assign costs to arcs (or edges) between nodes. The distance between nodes i and j is denoted by d_{ij} . Therefore, the objective function is the sum of all pairwise distances in the collection of assigned arcs. The column and row constraints dictate that each node is connected to exactly one and only one other node.

The objective function is the sum over all pairwise distances between nodes included in the mapping, where inclusion is determined by the binary solution matrix Y that has the following definition

$$y_{ij} = \begin{cases} 1 & \text{nodes } i \text{ and } j \text{ connected,} \\ 0 & \text{otherwise.} \end{cases} \quad (2)$$

Each row and each column of Y has a sum-to-one constraint, which means that each node in one collection is connected to exactly one other node in another disjoint collection. This problem assumes that the order (or size) of each collection is equal ($M = N$ in Fig. 3), so that a one-to-one assignment is possible. In the context of brain atlases, we will satisfy this requirement by adding artificial variables to our solution matrix Y . Pairwise distances between actual ROIs in a brain atlas and an artificial variable will be given a large constant value, so that ROIs in atlas A will preferentially map to another ROI in B if a mapping is possible. ROIs will be excluded from the mapping if they do not sufficiently overlap any ROI in the opposing atlas or if they map to an artificial variable. We show a diagram of atlas-atlas mapping (Fig. 4) that depicts ROIs as nodes and possible mappings as dashed lines between nodes in atlases A and B . Each possible mapping has a distance (d_{ij}) associated with its inclusion in the solution matrix Y . The solution is ultimately found by choosing connections (solid lines) between atlas ROIs so that each ROI in A is connected to exactly one ROI in B , which simultaneously minimizes the sum of all distances in the mapping. We also show how this mapping might look with respect to the actual brain atlases we consider in this manuscript (Fig. 5), where we have taken the unlabeled two-dimensional slices through

each atlas (Fig. 1) and assigned ROIs to each other based on similar location. Each of the atlases are in the Montreal Neurological Institute (MNI) coordinate space [8], which allows us to validly compare collections of voxels between them.

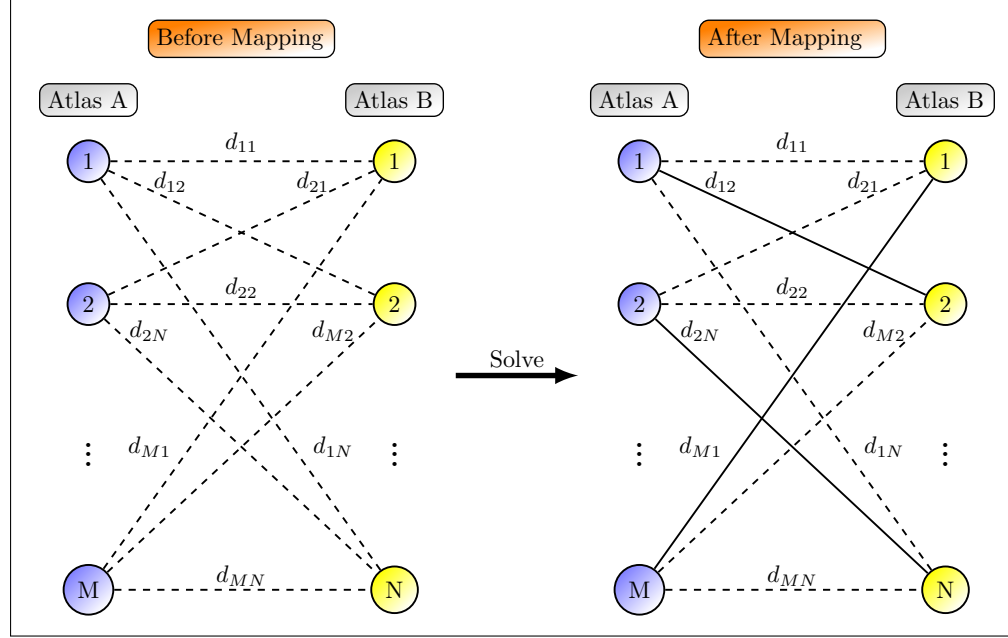


Fig 4. Assignment problem for brain atlas ROI-ROI mapping. Before the minimum distance pairwise mapping is found, all possible pairwise mappings are possible (dashed lines). Each ROI in atlas *A* must have exactly one partner in atlas *B*. After mapping, the minimum distance pairs are selected to give a one-to-one correspondence between ROIs (solid lines).

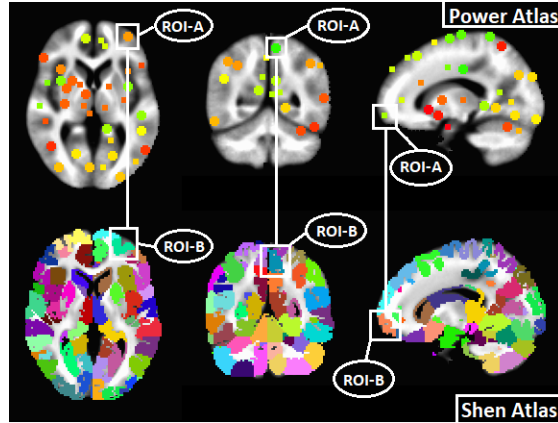


Fig 5. Visualization of mapping between Power and Shen atlas ROIs [5, 6]. ROIs that are in similar locations are potential partners in the resulting mapping from solving the assignment problem (Fig. 3). The Power atlas [5] is labeled atlas *A*, while the Shen atlas is labeled *B*.

2.3 Relative importance of ROIs

We load all subject-level resting-state fMRI (rs-fMRI) correlation matrices into a single matrix for our analysis (Fig. 6). Each column represents a single instance $i \in \mathcal{I}$ and each consecutive collection of $p - 1$ rows represents a single ROI $a \in \mathcal{A}$. We apply a Fisher r-to-z transform to all pairwise correlations prior to determining ROI importance.

$$\begin{array}{c}
\text{ROI}_1(a=1) \\
\text{ROI}_2(a=2) \\
\vdots \\
\text{ROI}_p(a=p)
\end{array}
\left\{ \begin{array}{c}
\begin{bmatrix} \hat{A}_{12}^{(1)} & \hat{A}_{12}^{(2)} & \hat{A}_{12}^{(3)} & \cdots & \hat{A}_{12}^{(m)} \\ \hat{A}_{13}^{(1)} & \hat{A}_{13}^{(2)} & \hat{A}_{13}^{(3)} & \cdots & \hat{A}_{13}^{(m)} \\ \vdots & \vdots & \vdots & \cdots & \vdots \\ \hat{A}_{1p}^{(1)} & \hat{A}_{1p}^{(2)} & \hat{A}_{1p}^{(3)} & \cdots & \hat{A}_{1p}^{(m)} \end{bmatrix} \\
\text{---} \\
\begin{bmatrix} \hat{A}_{21}^{(1)} & \hat{A}_{21}^{(2)} & \hat{A}_{21}^{(3)} & \cdots & \hat{A}_{21}^{(m)} \\ \hat{A}_{23}^{(1)} & \hat{A}_{23}^{(2)} & \hat{A}_{23}^{(3)} & \cdots & \hat{A}_{23}^{(m)} \\ \vdots & \vdots & \vdots & \cdots & \vdots \\ \hat{A}_{2p}^{(1)} & \hat{A}_{2p}^{(2)} & \hat{A}_{2p}^{(3)} & \cdots & \hat{A}_{2p}^{(m)} \end{bmatrix} \\
\text{---} \\
\begin{bmatrix} \hat{A}_{p1}^{(1)} & \hat{A}_{p1}^{(2)} & \hat{A}_{p1}^{(3)} & \cdots & \hat{A}_{p1}^{(m)} \\ \hat{A}_{p2}^{(1)} & \hat{A}_{p2}^{(2)} & \hat{A}_{p2}^{(3)} & \cdots & \hat{A}_{p2}^{(m)} \\ \vdots & \vdots & \vdots & \cdots & \vdots \\ \hat{A}_{p,p-1}^{(1)} & \hat{A}_{p,p-1}^{(2)} & \hat{A}_{p,p-1}^{(3)} & \cdots & \hat{A}_{p,p-1}^{(m)} \end{bmatrix}
\end{array} \right\} = \mathbf{X}$$

Fig 6. Organization based on brain regions of interest (ROIs) of resting-state fMRI correlation dataset consisting of transformed correlation matrices for m subjects. Each column corresponds to an instance (or subject) I_j and each subset of rows corresponds to the correlations for an ROI attribute (p sets). The notation $\hat{A}_{ak}^{(j)}$ represents the r-to-z transformed correlation between attributes (ROIs) a and $k \neq a$ for instance j .

We determine attribute importance using Nearest-neighbor Projected Distance Regression (NPDR) [4], which is a novel nearest-neighbor feature selection method that builds upon Relief-Based Algorithms (RBAs) [10, 11]. For binary response variables, like case-control outcomes, NPDR computes a standardized beta coefficient for a generalized linear model (GLM) (Fig. 7). The argument to the logit function is p_{ij}^{miss} , which is the probability that instances $i, j \in \mathcal{I}$ are in different phenotype classes. This argument models the binary outcome diff, which is given by the following

$$d_{ij}^{\text{miss}}(\vec{y}) = \begin{cases} 0 & y_i = y_j, \\ 1 & \text{else.} \end{cases} \quad (3)$$

For each coefficient β_a , a significant adjusted pseudo P value implies that the null hypothesis ($\beta_a \leq 0$) is rejected. The alternative hypothesis ($\beta_a > 0$) implies that the particular attribute $a \in \mathcal{A}$ may be important for classification.

In order to compute distances, we previously introduced a metric for time series-correlation based (ts-corr) data like rs-fMRI [3]. The one-dimensional projection (diff) onto a single ROI is define as follows

$$d_{ij}^{\text{ROI}}(a) = \sum_{k \neq a} |A_{ka}^{(i)} - A_{ka}^{(j)}|, \quad (4)$$

where $A_{ak}^{(i)}$ and $A_{ak}^{(j)}$ are the correlations between ROI a and ROI k for instances $i, j \in \mathcal{I}$, respectively. With this rs-fMRI diff, we define the pairwise distance between two instances $i, j \in \mathcal{I}$ as follows

$$D_{ij}^{\text{fMRI}} = \sum_{a \in \mathcal{A}} d_{ij}^{\text{ROI}}(a). \quad (5)$$

Using our attribute diff (Eq. 4), we compute standardized beta coefficients of the generalized linear model given by

$$\text{logit}(p_{ij}^{\text{miss}}) = \beta_0 + \beta_a d_{ij}^{\text{ROI}}(a) + \epsilon_{ij}, \quad \forall (i, j) \in \mathcal{N}(k), \quad (6)$$

which is the GLM that NPDR uses to compute standardized beta coefficients for binary outcomes with $d_{ij}(a)$ (Fig. 7) replaced by our diff for ROIs $d_{ij}^{\text{ROI}}(a)$ (Eq. 4). The

collection of all neighbor ordered pairs is denoted by $\mathcal{N}(k)$. This set is a function of k because we use a fixed- k approach in NPDR, where each target instance neighborhood has exactly k nearest neighbors.

**Nearest-neighbor Projected Distance
Regression (NPDR)**

For each $a \in \mathcal{A}$ do

$$\text{logit} \left(p_{ij}^{\text{miss}} \right) = \beta_0 + \beta_a d_{ij}(a) + \epsilon_{ij}, \quad \forall (i, j) \in \mathcal{N}(k)$$

Hypotheses

$$\left. \begin{array}{l} H_0 : \beta_a \leq 0 \\ H_1 : \beta_a > 0 \end{array} \right\} p_{\text{adj}} < 0.05 \Rightarrow \text{reject } H_0$$

Fig 7. Nearest-neighbor Projected Distance Regression for binary response (case-control) [4]. For each attribute $a \in \mathcal{A}$, we compute standardized beta coefficients for a generalized linear model, where the predictors ($d_{ij}(a) = |X_{ia} - X_{ja}|$) are one-dimensional projected distances (diffs) with respect to a particular attribute. The argument p_{ij}^{miss} is the probability that instances $i, j \in \mathcal{I}$ are in different phenotype classes. The logit function models the binary hit-miss phenotype projection (Eq. 3). Significant adjusted pseudo P values (p_{adj}) lead to the rejection of the null hypothesis $\beta_a \leq 0$. The set $\mathcal{N}(k)$ is the collection of all neighbor ordered pairs such that each target instances neighborhood has exactly k nearest neighbors.

We employ an adaptive- k algorithm called Gene-Wise Adaptive k (GWAK) that was originally developed for gene expression data [12] to determine the optimal k for each ROI in the two atlases we are analyzing. Although developed for gene expression data, this method can be used for other data types to which nearest-neighbor feature selection is applied. GWAK uses a greedy approach to optimize the relevance score for each attribute as a function of k (Fig. 8). For each attribute $a \in \mathcal{A}$, a relevance score is computed for each value of $k = 1, 2, \dots, m - 1$ using some nearest-neighbor feature selection algorithm. Each attribute is assigned the value of k that maximizes its relevance score. For noise attributes, scores do not change significantly as a function of k . On the other hand, the scores of relevant attributes will change significantly as a function of k . This implies that GWAK maximizes the probability of detecting relevant attributes when nearest-neighbor feature selection is utilized.

We have determined empirically with simulated data that cross-validation approaches for tuning k to optimally select relevant features do not perform well in nearest-neighbor feature selection as compared to GWAK. This is due largely to the fact that cross-validation optimizes test classification accuracy, which does not necessarily give the highest quality features. Partitioning data into training and test folds also limits the choice of k because the training data has only a subset of available instances in the full data set. Partitioning the data into training and test sets to choose a single value of k for the entire data set will cause the selection of a suboptimal k for a given relevant attribute, which could be detrimental to the quality of selected features. Our goal is to rank features in terms of relevance to a phenotype of interest as accurately as possible using a nearest-neighbor approach. Therefore, we use GWAK in our current analysis.

		Attributes				
		a_1	a_2	a_3	\dots	a_p
Neighbors (k)	1	-0.72	-0.98	0.85	\dots	-0.35
	2	0.67	0.60	-0.86	\dots	-0.12
	3	-0.52	0.83	0.12	\dots	0.61
	4	0.34	0.77	-0.42	\dots	0.84
	\vdots	\vdots	\vdots	\vdots	\dots	\vdots
	$m - 1$	0.11	-0.51	0.64	\dots	0.78
Winning Scores		0.67	0.83	0.85	\dots	0.84

Fig 8. Feature-wise adaptive- k method for choosing optimal values of k in nearest-neighbor feature selection. For each attribute $a \in \mathcal{A}$ and each value of $k = 1, 2, \dots, m - 1$, a score or weight is computed with a nearest-neighbor feature selection method like Relief-Based Algorithms (RBAs) or another similar method. Each feature is assigned the value of k that maximizes its importance score. Winning scores are then sorted in decreasing order and some fraction of the top scoring attributes are chosen for further analysis. We use the adjusted pseudo P values from NPDR to filter out attributes that are determined irrelevant to the phenotype. With NPDR, attribute scores are simply the standardized beta coefficients computed for the corresponding GLM (Eq. 6).

3 Results

In this section, we first give a pairwise mapping between the Power and Shen brain atlases. We describe the process of solving for a minimum distance one-to-one mapping. We then show which ROIs in the two atlases are determined important by NPDR, which are partitioned by those that are mapped and unmapped. Finally, we demonstrate the validity of important ROIs by referencing other analyses that have produced similar results.

3.1 Power and Shen atlas mapping

Since there are 277 and 278 ROIs in Power and Shen atlases, respectively, we first compute a distance matrix D that contains all pairwise distances between atlas ROIs. This gives us a 278×277 distance matrix to which we add a column of large numeric entries to represent distances from ROIs to an artificial variable. This makes the distance matrix square, which allows us to satisfy the one-to-one constraint of the Assignment Problem (Fig. 3). We used the open source statistical computing software **R** [13], which includes a package called **lpSolve** [14] for solving a variety of linear and integer programs. The **lpSolve** package contains the function `lp.assign()`, which simply takes a square distance matrix as input and produces solution matrix Y and an objective function value as output. For distance matrices comparable in dimension to D , the function elapses only a few seconds in run time.

We summarize the solution matrix from the Power-Shen ROI mapping given by `lp.assign()` (Table S3). Some of the entries in the solution matrix Y are extraneous,

which we define as one of the following: an ROI pair including an artificial variable, an ROI pair for which the Jaccard dissimilarity is maximal (e.g., $d^J(R_A, R_B) = 1$), or an ROI pair for which the Jaccard dissimilarity is simply larger than another pairwise dissimilarity. There is a total of 230 mapped ROIs between the two atlases, which leaves 47 and 48 unmapped ROIs in Power and Shen, respectively. Each Power atlas ROI exists in a single brain region (Tables S6-S7). Except for ROIs 265-277, each Power ROI is also part of some functional network, including but not limited to, the dorsal-Default Mode Network (dorsal-DMN), the visuospatial network, and the sensorimotor network. Each Shen ROI intersects multiple brain regions corresponding to Power ROIs. We used Power ROI overlap in order to assign brain regions to each Shen ROI (Tables S4-S5), however, we were not able to assign a brain region to all Shen ROIs because some of the ROIs do not intersect any Power ROIs. We partitioned the summary of Power and Shen ROI brain regions and functional networks by those that are mapped (Tables S4 and S6) and those that are unmapped (Tables S5 and S7). We also show a visualization of one atlas overlaid onto another (Fig. 9). Mapped ROIs from each atlas are highlighted to show relative spatial similarity (top of Fig. 9), which shows validation of the Assignment Problem solution. Unmapped ROIs from each atlas are highlighted to show relative spatial dissimilarity (bottom of Fig. 9), which similarly validates their categorization as extraneous mappings.

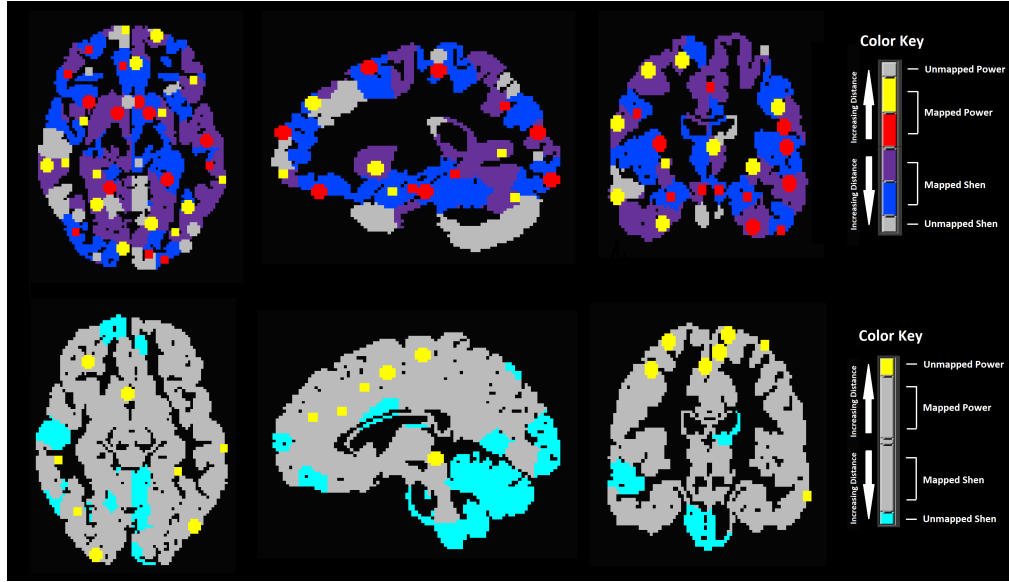


Fig 9. Visualization of mapped and unmapped ROIs from Power and Shen ROIs, respectively, from Assignment Problem solution. Two-dimensional slices from each atlas are overlaid on top of each other. The upper slices highlight the mapped ROIs from each atlas. The lower slices highlight the unmapped ROIs from each atlas.

Mapped ROIs are an indication of informational and spatial similarity shared by both atlases. Subject data that is derived from the mapped ROIs are highly correlated because each ROI pair shares voxels from which ROI time series are created. Unmapped ROIs in a single atlas may or may not intersect one of the mapped ROIs in another atlas. These unmapped ROIs indicate the most spatially unique aspects of each atlas relative to one another. Hence, unmapped ROIs should be considered for inclusion in a customized atlas if determined to be important for predicting the outcome.

3.2 Power and Shen atlas ROIs relevant to MDD

We used GWAK to determine the value of k that maximized the NPDR standardized beta coefficient β_a (Eq. 6) for each atlas ROI. ROIs with a Bonferroni adjusted pseudo P value less than 0.05 were categorized as important, while those with P values exceeding 0.05 were categorized as unimportant. Important mapped (Table 1) and unmapped (Table 2) Power ROIs correspond to several brain regions with known associations with MDD. The highest ranking mapped Power ROI is designated as 89 with respect to that atlas, which is in the right precuneus brain region in the dorsal default mode network (DMN). The precuneus in general, and the right precuneus in particular, has previously been associated with MDD [15–17]. We also summarize standardized beta coefficients, P values, brain regions, and functional networks for ROIs that were not significantly relevant to the outcome in the Power (Tables S1) and Shen (Table S2) atlases.

We have found that each of the important mapped Power ROI brain regions (Table 1) has been identified in several other studies regarding MDD: left middle temporal gyrus [18–20], left inferior temporal gyrus [21,22], left parahippocampal gyrus [21,23], right middle frontal gyrus [24,25], left cingulate gyrus [26,27], right superior frontal gyrus [28,29], right supramarginal gyrus [30,31], right orbital gyrus [22,32], right medial frontal gyrus [28,33], right caudate head [34,35], right inferior frontal gyrus [28,31], right superior temporal gyrus [36], left lingual gyrus [37,38], and right cuneus [39,40].

Similar to the collection of important mapped Power ROIs (Table 1), each important unmapped Power ROI brain region (Table 2) has been identified in other studies regarding MDD: left middle temporal gyrus [18–20], right middle temporal gyrus [22], right inferior parietal lobule [41], left medial frontal gyrus [25], left insula [42,43], right postcentral gyrus [42], and left cingulate gyrus [26,27].

NPDR-detected functional networks relevant to MDD have all been previously associated with the disorder: dorsal default mode network (DMN) [16,44–48], left executive control network (LECN) [49–51], right executive control network (RECN) [49–51], language network [52,53], primary visual network [53], sensorimotor network [53–55], and anterior salience network [56,57].

Nearly every Shen atlas ROI intersects multiple brain regions, as determined by Shen ROI intersection with Power ROIs that have unique brain region associations. We highlighted brain regions corresponding to mapped and unmapped important Shen ROIs (Tables 3–4) that were not detected as important with respect to the Power atlas. Some of the highlighted brain regions for significant ROIs may not actually be relevant because many of the detected Shen ROIs intersect important Power ROIs. Some of the brain regions intersected by important Shen ROIs, such as left culmen, left declive, right lingual gyrus, locus coeruleus, right declive, right parahippocampal gyrus, left inferior frontal gyrus, right uvula, left superior temporal gyrus, left precentral gyrus, left inferior parietal lobule, right superior parietal lobule, left middle occipital gyrus, left inferior occipital gyrus, right paracentral lobule, and left middle frontal, are the only brain regions associated with the particular Shen ROI. Almost all of these regions are relevant to MDD, but more investigation must be done to determine if the corresponding Shen ROI is important due to the incorporation of these brain regions or if significance is related to another associated brain region. For example, the most significant Shen ROI is labeled 243 (Table 3), which intersects the left inferior temporal gyrus, the left parahippocampal gyrus, and the left fusiform gyrus. The left inferior temporal gyrus and left parahippocampal gyrus are the brain regions that contain ROIs 4 and 77 in the Power atlas (Table 1), which are among the top 3 significant Power ROIs. This limits our ability to label the left fusiform gyrus as important with respect to these two atlases, however, this brain region has been associated with MDD in other studies [58,59].

Almost all brain regions intersected by important Shen ROIs, but not containing any important Power ROIs, are associated with MDD in other studies: left fusiform

gyrus [58,59], right insula [60,61], right lentiform nucleus [62,63], left superior frontal gyrus [25,28], left culmen [64,65], left declive [64,66], right lingual gyrus [37,38], left postcentral gyrus [42,67], left precentral gyrus [68,69], right inferior occipital gyrus [19,70], locus coeruleus [71,72], right declive [64,66], right fusiform gyrus [59,73], right inferior temporal gyrus [21], right parahippocampal gyrus [74,75], left paracentral lobule [22,76], left inferior frontal gyrus [28,77], right uvula [78], left inferior occipital gyrus [19], left middle occipital gyrus [79,80], left inferior parietal lobule [31,80], right superior parietal lobule [81,82], right paracentral lobule [22,83], right angular gyrus [84,85], left cuneus [77,86], left middle frontal gyrus [25,81], right precentral gyrus [30,68], and left uncus [87,88].

Considering that Power ROIs contain far fewer voxels than Shen ROIs, the likelihood of functionality for NPDR-detected Power ROIs (Tables 1-2) is probably larger. Shen ROIs intersect many brain regions, which mitigates our ability to determine relevance by brain region. However, NPDR-detected Shen ROIs (Table 3) that only intersect a single brain region, as determined by overlap with Power ROIs, may contain relevant regions not considered by the Power atlas. This could provide motivation for using both atlases separately or some combination of ROIs from each atlas, respectively, when classifying patients with MDD versus HC.

Table 1. Standardized beta coefficients, P values, and brain regions for important mapped Power atlas ROIs.

ROI	β_a	P Value	Brain Region	Func. Network
89	5.6464	5.87e-06	Right Precuneus	Dorsal DMN
4	5.3591	2.49e-05	Left Inferior Temporal Gyrus	LECN
77	5.1431	8.35e-05	Left Parahippocampal Gyrus	Dorsal DMN
181	4.7650	4.28e-04	Right Middle Frontal Gyrus	RECN
59	4.6523	7.55e-04	Left Cingulate Gyrus	Anterior Salience
180	4.6062	8.86e-04	Right Superior Frontal Gyrus	NA
204	4.5755	1.04e-03	Right Supramarginal Gyrus	RECN
5	4.5654	1.07e-03	Right Orbital Gyrus	Dorsal DMN
110	4.3227	3.08e-03	Right Medial Frontal Gyrus	Dorsal DMN
129	4.2442	4.23e-03	Left Middle Temporal Gyrus	Language
76	4.2390	4.60e-03	Right Medial Frontal Gyrus	Dorsal DMN
270	4.1885	5.29e-03	Right Caudate Head	NA
85	3.8958	1.72e-02	Right Inferior Frontal Gyrus	NA
82	3.8729	1.88e-02	Right Superior Temporal Gyrus	NA
160	3.7058	3.54e-02	Left Lingual Gyrus	Primary Visual
145	3.6940	3.76e-02	Right Cuneus	Primary Visual

Table 2. Standardized beta coefficients, P values, and brain regions for important unmapped Power atlas ROIs.

ROI	β_a	P Value	Brain Region	Func. Network
83	5.6804	4.92e-06	Left Middle Temporal Gyrus	LECN
128	4.9002	2.32e-04	Right Middle Temporal Gyrus	NA
192	4.0946	7.95e-03	Right Inferior Parietal Lobule	RECN
35	4.0692	8.59e-03	Left Medial Frontal Gyrus	Sensorimotor
73	4.0154	1.08e-02	Left Insula	NA
36	3.8673	2.19e-02	Right Postcentral Gyrus	Sensorimotor
213	3.6807	4.52e-02	Left Cingulate Gyrus	Anterior Salience

Table 3. Standardized beta coefficients, P values, and brain regions for important mapped Shen atlas ROIs. Brain regions were assigned to each Shen ROI based on overlap with known Power ROI brain regions. Brain regions for Shen ROIs that did not overlap any Power ROIs were assigned NA. Brain regions that did not show up in the list of important Power ROIs (Tables 1-2) are highlighted.

ROI	β_a	P Value	Brain Region
243	13.4157	2.41e-38	Left Inferior Temporal Gyrus, Left Parahippocampal Gyrus, Left Fusiform Gyrus
99	13.1216	1.09e-36	Right Middle Temporal Gyrus, Right Insula, Right Lenticular Nucleus
5	11.6413	7.29e-29	Right Postcentral Gyrus, Right Inferior Parietal Lobule
29	11.3464	2.06e-27	Right Postcentral Gyrus
277	9.5110	3.64e-19	Left Superior Frontal Gyrus, Left Medial Frontal Gyrus
178	9.1192	1.40e-17	Left Culmen, Left Declive
127	8.5795	1.66e-15	Right Lingual Gyrus
105	7.4976	1.03e-11	Right Medial Frontal Gyrus, Right Middle Frontal Gyrus, Right Superior Frontal Gyrus
262	7.4889	1.10e-11	Left Postcentral Gyrus, Left Precentral Gyrus, Left Medial Frontal Gyrus
96	7.0001	3.94e-10	Right Inferior Occipital Gyrus, Right Lingual Gyrus
239	6.9550	5.39e-10	Locus Coeruleus
104	6.8045	1.54e-09	Right Declive
217	6.6554	4.25e-09	Left Parahippocampal Gyrus, Left Fusiform Gyrus
238	6.4225	2.00e-08	Left Middle Temporal Gyrus
83	6.3879	2.55e-08	Right Superior Temporal Gyrus
57	6.3269	3.71e-08	Right Inferior Parietal Lobule, Right Postcentral Gyrus
7	6.2803	5.01e-08	Right Middle Frontal Gyrus, Right Precentral Gyrus
12	6.2222	7.29e-08	Right Lingual Gyrus, Right Cuneus
32	6.1985	8.42e-08	Right Precentral Gyrus, Right Postcentral Gyrus
102	6.1316	1.28e-07	Right Inferior Occipital Gyrus, Right Middle Occipital Gyrus
19	6.0343	2.34e-07	Right Fusiform Gyrus, Right Middle Temporal Gyrus, Right Inferior Temporal Gyrus
21	6.0037	2.83e-07	Right Cingulate Gyrus, Right Precuneus
202	5.7008	1.74e-06	Left Declive, Left Culmen
136	5.6781	1.98e-06	Right Parahippocampal Gyrus
253	5.5841	3.40e-06	Right Medial Frontal Gyrus, Left Medial Frontal Gyrus, Left Paracentral Lobule
113	5.4798	6.17e-06	Right Culmen, Right Parahippocampal Gyrus
271	5.3379	1.41e-05	Left Medial Frontal Gyrus
215	5.2170	2.86e-05	Left Inferior Frontal Gyrus
130	5.1917	2.99e-05	Right Uvula
257	5.0391	6.68e-05	Left Lingual Gyrus, Left Inferior Occipital Gyrus, Left Middle Occipital Gyrus
237	5.0153	7.61e-05	Left Superior Temporal Gyrus, Left Precentral Gyrus
245	5.0136	7.68e-05	Left Superior Temporal Gyrus, Left Inferior Parietal Lobule

Continued on next page

Table 3 – continued from previous page

ROI	β_a	P Value	Brain Region
80	4.7380	3.07e-04	Right Superior Parietal Lobule, Right Precuneus
247	4.7039	3.63e-04	Left Middle Occipital Gyrus, Left Inferior Occipital Gyrus
55	4.5641	7.10e-04	Right Paracentral Lobule, Left Cingulate Gyrus, Right Medial Frontal Gyrus
8	4.5240	8.59e-04	Right Postcentral Gyrus
45	4.4630	1.14e-03	Right Medial Frontal Gyrus, Right Postcentral Gyrus
24	4.4623	1.15e-03	Right Supramarginal Gyrus, Right Angular Gyrus, Right Inferior Parietal Lobule
84	4.4571	1.18e-03	Left Cuneus, Right Precuneus, Right Cuneus
121	4.3935	1.58e-03	Right Lingual Gyrus
206	4.1698	4.32e-03	Left Inferior Frontal Gyrus
38	4.1499	4.83e-03	Right Uvula
193	4.1029	5.74e-03	Left Middle Frontal Gyrus
28	4.0366	7.66e-03	Right Postcentral Gyrus, Right Precentral Gyrus
213	3.9603	1.05e-02	Left Uncus, Left Parahippocampal Gyrus
147	3.8788	1.48e-02	Left Middle Occipital Gyrus, Left Middle Temporal Gyrus
87	3.8019	2.01e-02	Right Fusiform Gyrus, Right Middle Temporal Gyrus, Right Middle Occipital Gyrus
218	3.6315	3.96e-02	Left Precentral Gyrus
103	3.5907	4.64e-02	Right Inferior Frontal Gyrus

Table 4. Standardized beta coefficients, P values, and brain regions for important unmapped Shen atlas ROIs. Brain regions were assigned to each Shen ROI based on overlap with known Power ROI brain regions. Brain regions for Shen ROIs that did not overlap any Power ROIs were assigned NA.

ROI	β_a	P Value	Brain Region
49	9.5173	3.40e-19	NA
3	9.3489	1.67e-18	Right Medial Frontal Gyrus
76	9.0332	3.04e-17	NA
79	9.0313	3.08e-17	NA
175	8.4150	6.68e-15	Right Declive
219	7.8334	7.68e-13	NA
35	7.7575	1.39e-12	Right Middle Temporal Gyrus
231	7.5458	7.13e-12	Left Declive, Right Declive, Left Lingual Gyrus
174	7.5352	7.72e-12	NA
256	7.3053	4.32e-11	Left Declive
141	7.2127	8.50e-11	NA
13	6.2918	4.65e-08	NA
158	6.2916	4.67e-08	NA
196	5.9340	4.33e-07	NA
126	4.9343	1.15e-04	Right Uvula
31	4.8789	1.52e-04	NA
70	4.8009	2.25e-04	NA
115	4.6691	4.33e-04	Locus Coeruleus

4 Discussion

In this work, we have presented a method for determining the minimum distance one-to-one mapping between pairs of ROIs in two fMRI brain atlases. This method uses the framework of the Assignment Problem (Fig. 3), and naturally employs the Jaccard metric (Eq. 1) to compute distances between pairs of ROIs. For any pair of fMRI brain atlases in the same coordinate space, we can compute a solution to the corresponding Assignment Problem. Mapped ROIs represent the closest spatial pairing between atlases, whereas unmapped ROIs represent relative spatial uniqueness in each respective atlas. We found a mapping between the Power [5] and Shen [6] fMRI brain atlases, which contains 230 pairs of mapped ROIs (Table S3) between the two atlases. This mapping excludes 47 ROIs from the Power atlas (Table S7) and 48 ROIs from the Shen atlas (Table S5). Because each Power ROI coincides with a single brain region (Tables S6 and S7), we were able to assign brain regions to each of the mapped (Table S4) and unmapped (Table S5) Shen ROIs based on overlap with Power ROIs.

Our method of assigning importance to ROIs with Nearest-neighbor Projected Distance Regression (NPDR) [4] is novel not only because we have introduced a new attribute diff metric (Eq. 4) specifically for this context so that pairwise distances (Eq. 5) can be computed between any two instances $i, j \in \mathcal{I}$, but also because we have used nearest-neighbor feature selection to assign variable importance at the ROI level. In doing this, we have the ability to compute relevance scores and a pseudo P value for each ROI in a given atlas. This allows us to compare and contrast ROIs in two or more atlases with respect to their ability to accurately classify a given outcome. We have considered ROI relevance to MDD in our analysis, but our work could easily be extended to other dichotomous (or continuous) outcomes.

The outcome in our data consists of 40 healthy controls and 171 subjects with MDD, which is heavily imbalanced. Relief-based algorithms have typically dealt with imbalance by using the same number of hits and misses with respect to target instances to compute attribute scores [11]. Running NPDR on simulated data with imbalanced outcome, we have seen empirically that attribute quality is optimized by allowing each target instance to have a neighborhood that consists of the k closest hits or misses. That is, each target instance's neighborhood is chosen without regard to class label. This implies that each neighborhood can have a different proportion of hits and misses, however, results from simulated data indicate that this optimizes the quality of selected features.

We used GWAK [12] to assign scores to each ROI, which is also a novel application. When a nearest-neighbor feature selection algorithm is applied to data with a dichotomous outcome, GWAK optimizes the quality of feature rankings with respect to their scores. In the context of nearest-neighbor feature selection, we have observed that GWAK performs much better than cross-validation approaches that split the data into training and test folds. The superiority of GWAK is based on the fact that it optimizes outcome relevance scores for all attributes, which significantly affects only those attributes that are relevant to the given outcome. The average score of irrelevant attributes remains approximately unchanged as a function of the number of nearest neighbors k , whereas scores of relevant attributes can dramatically change with the choice of k . By optimizing k for each feature, we maximize the probability of detecting relevant attributes.

NPDR-GWAK detected a total of 23 important Power ROIs (Tables 1-2) and 66 important Shen ROIs (Tables 3-4). We have found that nearly all detected ROIs have been formerly associated with MDD, which at least to some degree implies that our method of determining ROI importance using a novel nearest-neighbor approach is valid. Power ROIs are localized to single brain regions and functional networks, which allows for more precision in the identification of MDD-relevant localities within the brain. There are many more significant Shen ROIs for our MDD-HC outcome, but each of these ROIs may intersect multiple brain regions. There are some important Shen ROIs that

intersect only a single Power ROI and corresponding brain region (Table 3-4). More work
needs to be done to determine what aspects of these ROIs make them relevant to MDD.
However, we have shown that nearly all of the highlighted brain regions (Tables 3-4)
associated with important Shen ROIs that simultaneously do not exist among important
Power ROIs have been correlated with MDD in other studies. This further supports the
validity of our NPDR-GWAK method for assigning importance to ROIs.

The MDD outcome group includes both subjects with only MDD and others with
MDD and an anxiety disorder as well. It is well known that there is a high degree of
comorbidity between MDD and anxiety disorders [89–91]. This enhanced comorbidity
could be the result of overlapping characteristics between the two disorders from di-
agnostic tests [89]. We have primarily been concerned with MDD in our analysis, but
the combination of subjects with only MDD and those with both MDD and anxiety
could be a potential drawback. Combination of these two distinct groups of MDD
subjects was done in order to increase statistical power, so that our ability to detect
MDD-relevant ROIs was maximized. More work needs to be done to determine whether
the inclusion of subjects with both MDD and anxiety is a significant confounding factor
for the determination of MDD-relevant ROIs.

We have also shown that spatial similarity does not necessarily imply similarity in
relevance. For example, Shen ROI 21 (Table 3) and Power ROI 89 (Table 1) form the
only mapped pair in the collection of important ROIs from the two atlases. Aside from
these two, all of the other mapped ROIs are missing their spatial counterpart (Table S3)
among the list of important ROIs (Tables 1 and 3). Important unmapped ROIs represent
unique potential MDD-relevance among the Power and Shen atlases. A MDD-relevant
atlas could possibly be created by incorporating a combination of important mapped and
unmapped ROIs from both atlases. This custom atlas would include the MDD-relevant
spatial coverage from both Power and Shen atlases. Our method of determining a spatial
mapping between atlases and also assigning phenotype relevance to ROIs can be applied
to any pair of fMRI atlases, which allows for the creation of multiple new atlases with
the purpose of analyzing the phenotype of interest.

References

1. César Caballero Gaudes and Richard C. Reynolds. Methods for cleaning the
BOLD fMRI signal. *NeuroImage*, 154:128–149, December 2017.
2. Trang T Le, W Kyle Simmons, Masaya Misaki, Jerzy Bodurka, Bill C White,
Jonathan Savitz, and Brett A McKinney. Differential privacy-based evapora-
tive cooling feature selection and classification with relief-f and random forests.
Bioinformatics, 33(18):2906–2913, 2017.
3. Bryan A. Dawkins, Trang T. Le, and Brett A. McKinney. Theoretical properties
of nearest-neighbor distance distributions and novel metrics for high dimensional
bioinformatics data. *Under Review*, 2019.
4. Trang T. Le, Bryan A. Dawkins, and Brett A. McKinney. Nearest-neighbor
Projected-Distance Regression (NPDR) detects network interactions and controls
for confounding and multiple testing. *Under Review*, 2019.
5. Jonathan D Power, Alexander L Cohen, Stephen M Nelson, Gagan S Wig,
Kelly Anne Barnes, Jessica A Church, Alecia C Vogel, Timothy O Laumann,
Fran M Miezin, Bradley L Schlaggar, and Steven E Peterson. Functional network
organization of the human brain. *Neuron*, 72(4):665–678, November 2011.

6. X. Shen, F. Tokoglu, X. Papademetris, and R. T. Constable. Groupwise whole-
brain parcellation from resting-state fMRI data for network node identification.
Neuroimage, (0):403–415, November 2013.
7. RW Cox. AFNI: software for analysis and visualization of functional magnetic
resonance neuroimages. *Computational Biomedical Research*, 29(3):162–173, June
1996.
8. DL Collins, P Neelin, and TM Peters. Automatic 3D intersubject registration
of MR volumetric data in standardized Talairach space. *Journal of Computer
Assisted Tomography*, 18(2):192–205, April 1994.
9. David W. Pentico. Assignment problems: A golden anniversary survey. *European
Journal of Operational Research*, 176:774–793, November 2007.
10. Marko Robnik Šikonja and Igor Kononenko. Theoretical and Empirical Analysis
of ReliefF and RReliefF. *Machine Learning*, 53:23 – 69, February 2003.
11. Ryan J. Urbanowicz, Randal S. Olson, Peter Schmitt, Melissa Meeker, and Jason H.
Moore. Benchmarking relief-based feature selection methods for bioinformatics
data mining. *Journal of Biomedical Informatics*, 85:168–188, 2018.
12. Brett A McKinney, Bill C White, Diane E Grill, Peter W Li, Richard B Kennedy,
Gregory A Poland, and Ann L Oberg. ReliefSeq: a gene-wise adaptive-K nearest-
neighbor feature selection tool for finding gene-gene interactions and main effects
in mRNA-Seq gene expression data. *PloS one*, 8(12):e81527, 2013.
13. R Core Team. *R: A Language and Environment for Statistical Computing*. R
Foundation for Statistical Computing, Vienna, Austria, 2017.
14. Michel Berkelaar and others. *lpSolve: Interface to 'Lp_solve' v. 5.5 to Solve
Linear/Integer Programs*, 2015. R package version 5.6.13.
15. Wei Cheng, Edmund T. Rolls, Jiang Qiu, Deyu Yang, Hongtao Ruan, Dongtao
Wei, Libo Zhao, Jie Meng, Peng Xie, and Jianfeng Feng. Functional Connectivity
of the Precuneus in Unmedicated Patients With Depression. *Biological Psychiatry:
Cognitive Neuroscience and Neuroimaging*, 3:1040–1049, December 2018.
16. Arpan Dutta, Shane McKie, Darragh Downey, Emma Thomas, Gabriella Juhasz,
Danilo Arnone, Rebecca Elliot, Steve Williams, J. F. William Deakin, and Ian
M. Anderson. Regional default mode network connectivity in major depressive
disorder: modulation by acute intravenous citalopram. *Translational Psychiatry*,
9(116), 2019.
17. Liu CH, Ma X, Yuan Z, Song LP, Jing B, Lu Hy, Tang LR, Fan J, Walter M, Liu
CZ, Wang L, and Wang CY. Decreased Resting-State Activity in the Precuneus Is
Associated With Depressive Episodes in Recurrent Depression. *J Clin Psychiatry*,
78(4):372–382, April 2017.
18. Jinping Xu, Jiaojian Wang, Tongjian Bai, Xiaodong Zhang, Tian Li, Qingmao Hu,
Hongming Li, Li Zhang, Qiang Wei, Yanghua Tian, and Kai Wang. Electrocon-
vulsive Therapy Induces Cortical Morphological Alterations in Major Depressive
Disorder Revealed with Surface-Based Morphometry Analysis. *International
Journal of Neural Systems*, 29(7), 2019.

19. Bradley S. Peterson, Virginia Warner, Ravi Bansal, Hongtu Zhu, Xuejun Hao, 442
Jun Liu, Kathleen Durkin, Phillip B. Adams, Priya Wickramaratne, and Myrna 443
M. Weissman. Cortical thinning in persons at increased familial risk for major 444
depression. *PNAS*, 106(15):6273–6278, April 2009. 445
20. Syeda F. Husain, Tong-Boon Tang, Rongjun Yu, Wilson W. Tam, Bach Tran, 446
Travis T. Quek, Shi-Hui Hwang, Cheryl W. Chang, Cyrus S. Ho, and Roger 447
C. Ho. Cortical haemodynamic response measured by functional near infrared 448
spectroscopy during a verbal fluency task in patients with major depression and 449
borderline personality disorder. *EBioMedicine*, November 2019. 450
21. Mahdi Ramezani, Ingrid Johnsrude, Abtin Rasouljan, Rachael Bosma, Ryan 451
Tong, and Tom Hollenstein. Temporal-lobe morphology differs between healthy 452
adolescents and those with early-onset of depression. *NeuroImage: Clinical*, 453
6:145–155, August 2014. 454
22. Edmund T. Rolls, Wei Cheng, and Matthieu Gilson et al. Effective Connectivity 455
in Depression. *Biological Psychiatry: Cognitive Neuroscience and Neuroimaging*, 456
2017. 457
23. Ling-Li Zeng, Hui Shen, Li Liu, Lubin Wang, Baojuan Li, Peng Fang, Zongtan 458
Zhou, Yaming Li, and Dewen Hu. Identifying major depression using whole-brain 459
functional connectivity: a multivariate pattern analysis. *BRAIN: A JOURNAL 460
OF NEUROLOGY*, 135:1498–1507, March 2012. 461
24. Stephanie Reynolds, Normand Carrey, Natalia Jaworska, Lisa Marie Langevin, 462
Xiao-Ru Yang, and Frank P MacMaster. Cortical thickness in youth with major 463
depressive disorder. *BMC Psychiatry*, 14(83), 2014. 464
25. Paul B. Fitzgerald, Angela R. Laird, Jerome Maller, and Zafiris J. Daskalakis. A 465
Meta-Analytic Study of Changes in Brain Activation in Depression. *Hum Brain 466
Mapp*, 29(6):683–695, June 2008. 467
26. Clement Hamani, Helen Mayberg, Scellig Stone, Adrian Laxton, Suzanne Haber, 468
and Andres M. Lozano. The Subcallosal Cingulate Gyrus in the Context of Major 469
Depression. *BIOL PSYCHIATRY*, 69:301–308, 2011. 470
27. ME McLaren, SM Szymkowicz, A O’Shea, AJ Woods, SD Anton, and VM Dotson. 471
Dimensions of depressive symptoms and cingulate volumes in older adults. *Transl 472
Psychiatry*, 6, April 2016. 473
28. H Tao, S Guo, T Ge, KM Kendrick, Z Xue, Z Liu, and J Feng. Depression 474
uncouples brain hate circuit. *Molecular Psychiatry*, 18:101–111, October 2013. 475
29. Giacomo Salvatore, Allison C. Nugent, Herve Lemaitre, David A. Luckenbaugh, 476
Ruth Tinsley, Dara M. Cannon, Alexander Neumeister, Carlos A. Zarate Jr., 477
and Wayne C. Drevets. Prefrontal cortical abnormalities in currently depressed 478
versus currently remitted patients with major depressive disorder. *Neuroimage*, 479
54(4):2643–2651, February 2011. 480
30. Daihui Peng, Feng Shi, Gang Li, Drew Fralick, Ting Shen, Meihui Qiu, Jun Liu, 481
Kaida Jiang, Dinggang Shen, and Yiru Fang. Surface Vulnerability of Cerebral 482
Cortex to Major Depressive Disorder. *PLoS ONE*, March 2015. 483
31. Zhe Tu, Yuan Yuan Jia, Tao Wang, Hang Qu, Jun Xi Pan, Jie Jie, Xiao Yan Xu, 484
Hai Yang Wang, and Peng Xie. Modulatory interactions of resting-state brain 485
functional connectivity in major depressive disorder. *Neuropsychiatric Disease 486
and Treatment*, 14:2461–2472, 2018. 487

32. Rui Yan, ShiWan Tao, HaiYan Liu, Yu Chen, JiaBo Shi, YuYin Yang, RongXin Zhu, ZhiJian Yao, and Qing Lu. Abnormal Alterations of Regional Spontaneous Neuronal Activity in Inferior Frontal Orbital Gyrus and Corresponding Brain Circuit Alterations: A Resting-State fMRI Study in Somatic Depression. *Frontiers in Psychiatry*, 10(267), April 2019.
33. Cédric Lemogne, Guillaume le Bastard, Helen Mayberg, Emmanuelle Volle, Loretxu Bergouignan, Stéphane Lehericy, Jean-François Allilaire, and Philippe Fossati. In search of the depressive self: extended medial prefrontal network during self-referential processing in major depression. *SCAN*, 4:305–312, March 2009.
34. Diego A. Pizzagalli, Avram J. Holmes, Daniel G. Dillon, Elena L. Goetz, Jeffrey L. Birk, Ryan Bogdan, Darin D. Dougherty, Dan V. Iosifescu, Scott L. Rauch, and Maurizio Fava. Reduced Caudate and Nucleus Accumbens Response to Rewards in Unmedicated Subjects with Major Depressive Disorder. *Am J Psychiatry*, 166(6):702–710, June 2009.
35. Robyn Bluhm, Peter Williamson, Ruth Lanius, Jean Théberge, Maria Densmore, Robert Bartha, Richard Neufeld, and Elizabeth Osuch. Resting state default-mode network connectivity in early depression using a seed region-of-interest analysis: Decreased connectivity with caudate nucleus. *Psychiatry and Clinical Neuroscience*, 63:754–761, August 2009.
36. Lisa A. Pan, Lisa Ramos, AnnaMaria Segreti, David A. Brent, and Mary L. Phillips. Right superior temporal gyrus volume in adolescents with a history of suicide attempt. *The British Journal of Psychiatry*, 206:339–340, 2015.
37. JeYoung Jung, June Kang, Eunsoo Won, Kichun Nam, Min-Soo Lee, Woo Suk Tae, and Byung-Joo Ham. Impact of lingual gyrus volume on antidepressant response and neurocognitive functions in Major Depressive Disorder: A voxel-based morphometry study. *Journal of Affective Disorders*, 169:179–187, August 2014.
38. Baptiste Couvy Duchesne, Lachlan T. Strike, Greig I. de Zubicaray, Katie L. McMahon, Paul M. Thompson, Ian B. Hickie, Nicholas G. Martin, and Margaret J. Wright. Lingual Gyrus Surface Area Is Associated with Anxiety-Depression Severity in Young Adults: A Genetic Clustering Approach. *Disorders of the Nervous System*, 5(1), February 2018.
39. Tongjian Bai, Meidan Zu, Yang Chen, Wen Xie, Chunlan Cai, Qiang Wei, Gong-Jun Ji, Yanghua Tian, and Kai Wang. Decreased Connection Between Reward Systems and Paralimbic Cortex in Depressive Patients. *Frontiers in Neuroscience*, 12(462), July 2018.
40. Shengnan Wei, Miao Chang, Ran Zhang, Xiaowei Jiang, Fei Wang, and Yanqing Tang. Amygdala functional connectivity in female patients with major depressive disorder with and without suicidal ideation. *Ann Gen Psychiatry*, 17(37), 2018.
41. Rebecca E. Cooney, Jutta Joorman, Fanny Eugène, Emily L. Dennis, and Ian H. Gotlib. Neural correlates of rumination in depression. *Cognitive, Affective, & Behavioral Neuroscience*, 10(4):470–478, 2010.
42. L Schmaal et al. Cortical abnormalities in adults and adolescents with major depression based on brain scans from 20 cohorts worldwide in the ENIGMA Major Depressive Disorder Working Group. *Molecular Psychiatry*, 22:900–909, May 2017.

43. Wenbin Li, Ziqi Chen, Min Wu, Hongyan Zhu, Lei Gu, Youjin Zhao, Weihong Kuang, Feng Bi, Graham J. Kemp, and Qiyong Gong. Characterization of brain blood flow and the amplitude of low-frequency fluctuations in major depressive disorder: A multimodal meta-analysis. *Journal of Affective Disorders*, 210:303–311, December 2017.
44. J. Paul Hamilton, Madison Farmer, Phoebe Fogelman, and Ian H. Gotlib. Depressive Rumination, the Default-Mode Network, and the Dark Matter of Clinical Neuroscience. *Biol Psychiatry*, 78(4):224–230, August 2015.
45. Chao-Gan Yan et al. Reduced default mode network functional connectivity in patients with recurrent major depressive disorder. *PNAS*, 116(18):9078–9083, April 2019.
46. Giannis Lois and Michéle Wessa. Differential association of default mode network connectivity and rumination in healthy individuals and remitted MDD patients. *Social Cognitive and Affective Neuroscience*, pages 1792–1801, July 2016.
47. Wenbin Guo, Feng Liu, Jian Zhang, Zhikun Zhang, Liuyu Yu, Jianrong Liu, Huafu Chen, and Changqing Xiao. Abnormal Default-Mode Network Homogeneity in First-Episode, Drug-Naive Major Depressive Disorder. *PLoS ONE*, 9(3), March 2014.
48. Vinod Menon. Large-scale brain networks and psychopathology: a unifying triple network model. *Trends in Cognitive Sciences*, 2011.
49. Qinghua Zhao, Zarnawab N. K. Swati, Hichem Metmer, Xiaoshuang Sang, and Jianfeng Lu. Investigating executive control network and default mode network dysfunction in major depressive disorder. *Neuroscience Letters*, 701, March 2019.
50. Kristen K. Ellard, Jared P. Zimmerman, Navneet Kaur, Koene R. A. Van Dijk, Joshua L. Roffman, Andrew A. Nierenberg, Darin D. Dougherty, Thilo Deckersbach, and Joan A. Camprodon. Functional Connectivity Between Anterior Insula and Key Nodes of Frontoparietal Executive Control and Salience Networks Distinguish Bipolar Depression From Unipolar Depression and Healthy Control Subjects. *Biological Psychiatry: Cognitive Neuroscience and Neuroimaging*, 3:473–484, May 2018.
51. Li Liu, Ling-Li Zeng, Yaming Li, Qiongmin Ma, Baojuan Li, Hui Shen, and Dewen Hu. Altered Cerebellar Functional Connectivity with Intrinsic Connectivity Networks in Adults with Major Depressive Disorder. *PLoS ONE*, 7(6), June 2012.
52. Douglas H. Schultz, Takuya Lto, Levi I. Solomyak, Richard H. Chen, Ravi D. Mill, Alan Antecvic, and Michael W. Cole. Global connectivity of the frontoparietal cognitive control network is related to depression symptoms in the general population. *Network Neuroscience*, April 2018.
53. Xing-jie Wu, Ling-Li Zeng, Hui Shen, Lin Yuan, Jian Qin, Peng Zhang, and Dewen Hu. Functional network connectivity alterations in schizophrenia and depression. *Psychiatry Research: Neuroimaging*, 263:113–120, March 2017.
54. Dongmei Zhi, Vince D. Calhoun, Luxian Lv, Xiaohong Ma, Qing Ke, Zening Fu, Yuhui Du, Yongfeng Yang, Xiao Yang, Miao Pan, Shile Qi, Rongtao Jiang, Qingbao Yu, and Jing Sui. Aberrant Dynamic Functional Network Connectivity and Graph Properties in Major Depressive Disorder. *Frontiers in Psychiatry*, 9(339), July 2018.

55. Chuanjun Zhuo, Jiajia Zhu, Chunli Wang, Hongru Qu, Xiaolei Ma, and Wen Qin. Different spatial patterns of brain atrophy and global functional connectivity impairments in major depressive disorder. *Brain Imaging and Behavior*, 11:1678–1689, 2017.
56. Magdalena Sikora, Joseph Heffernan, Erich T. Avery, Brian J. Mickey, Jon-Kar Zubieta, and Marta Pecina. Salience Network Functional Connectivity Predicts Placebo Effects in Major Depression. *Biol Psychiatry Cogn Neurosci Neuroimaging*, 1(1), January 2017.
57. Xiang Wang, Dost Öngür, Randy P. Auerbach, and Shuqiao Yao. Cognitive Vulnerability to Major Depression: View from the Intrinsic Network and Cross-network Interactions. *Harvard Review of Psychiatry*, 24(3), June 2016.
58. Sarina J. Iwabuchi, Rajeev Krishnadas, Chunbo Li, Dorothee P. Auer, Joaquim Radua, and Lena Palaniyappan. Localized connectivity in depression: A meta-analysis of resting state functional imaging studies. *Neuroscience and Biobehavioral Reviews*, 51:77–86, January 2015.
59. Marijn C. W. Kroes, Michael D. Rugg, Matthew G. Whalley, and Chris R. Brewin. Structural brain abnormalities common to posttraumatic stress disorder and depression. *J Psychiatry Neurosci*, 36(4), October 2011.
60. Jason Avery, Wayne C. Drevets, Scott Moseman, Jerzy Bodurka, and W. Kyle Simmons. Major depressive disorder is associated with abnormal interoceptive activity and functional connectivity in the insula. *Biol Psychiatry*, 76(3):258–266, August 2014.
61. Sarina J. Iwabuchi, Daihui Peng, Yiru Fang Kaida Jiang, Elizabeth B Liddle, Peter F. Liddle, and Lena Palaniyappan. Alterations in effective connectivity anchored on the insula in major depressive disorder. *European Neuropsychopharmacology*, 24:1784–1792, August 2014.
62. Su Lui, Laura M. Parkes, Xiaoqi Huang, Ke Zou, Raymond C. K. Chan, Hong Yang, Ling Zou, Dongming Li, Hehan Tang, Tijiang Zhang, Xiuli Li, Yi Wei, Long Chen, Xueli Sun, Graham J. Kemp, and Qi-Yong Gong. Altered Cerebral Perfusion Measured with Arterial Spin-labeling MR Imaging. *Neuroradiology*, 251(2), May 2009.
63. Katharina Helm, Kathrin Viol, Thomas M Weiger, Peter A Tass, Christian Grefkes, Damir del Monte, and Günter Schiepek. Neuronal connectivity in major depressive disorder: a systematic review. *Neuropsychiatric Disease and Treatment*, 14:2715–2737, 2018.
64. Liang Su, Yiyun Cai, Yifeng Xu, Anirban Dutt, Shenxun Shi, and Elvira Bramon. Cerebral metabolism in major depressive disorder: a voxel-based meta-analysis of positron emission tomography studies. *BMC Psychiatry*, 14(321), 2014.
65. T Yamamura, Y Okamoto, G Okada, Y Takaishi, M Takamura, A Mantani, A Kurata, Y Otagaki, H Yamashita, and S Yamawaki. Association of thalamic hyperactivity with treatment-resistant depression and poor response in early treatment for major depression: a resting-state fMRI study using fractional amplitude of low-frequency fluctuations. *Transl Psychiatry*, 6, March 2016.
66. Wei-Che Lin, Kun-Hsien Chou, Hsiu-Ling Chen, Chu-Chung Huang, Cheng-Hsien Lu, Shau-Hsuan Li, Ya-Ling Wang, Yu-Fan Cheng, Ching-Po Lin, and Chien-Chih

- Chen. Structural deficits in the emotion circuit and cerebellum are associated with depression, anxiety and cognitive dysfunction in methadone maintenance patients: A voxel-based morphometric study. *Psychiatry Research: Neuroimaging*, 201:89–97, May 2012.
67. Huifeng Zhang, Meihui Qiu, Lei Ding, David Mellor, Gang Li, Ting Shen, and Daihui Peng. Intrinsic gray-matter connectivity of the brain in major depressive disorder. *Journal of Affective Disorders*, 251:78–85, March 2019.
68. Noa Tsujii, Wakako Mikawa, Emi Tsujimoto, Toru Adachi, Atsushi Niwa, Hisae Ono, and Osamu Shirakawa. Reduced left precentral regional responses in patients with major depressive disorder and history of suicide attempts. *PLoS ONE*, April 2017.
69. Ting Shen, Cao Li, Biao Wang, Wei-min Yang, Chen Zhang, Zhiguo Wu, Mei-hui Qiu, Jun Liu, Yi-feng Xu, and Dai-hui Peng. Increased Cognition Connectivity Network in Major Depression Disorder: A fMRI Study. *Psychiatry Investig*, 12(2):227–234, February 2015.
70. Stuart M. Grieve, Mayuresh S. Korgaonkar, Stephen H. Koslow, Evian Gordon, and Leanne M. Williams. Widespread reductions in gray matter volume in depression. *NeuroImage: Clinical*, 3:332–339, September 2013.
71. Bin Wang, Ying Wang, Qiong Wu, Hong-ping Huang, and Shao Li. Effects of $\alpha 2A$ Adrenoreceptors on Norepinephrine Secretion from the Locus Coeruleus during Chronic Stress-Induced Depression. *Frontiers in Neuroscience*, May 2017.
72. Kenjiro Seki, Satomi Yoshida, and Manoj Kumar Jaiswal. Molecular mechanism of noradrenaline during the stress-induced major depressive disorder. *Neural Regeneration Research*, 13(7):1159–1169, October 2019.
73. Chen Lin, Yun Bian, Xiaole Han, Li Chen, Yu Zhu, and Dachun Chen. Gray Matter Reduction in Currently Depressed Patients of Major Depressive Disorder: A Meta-Analysis. *Neuropsychiatry (London)*, 7(5):596–605, 2017.
74. Vera Zamoscik, Silke Huffziger, Ulrich Ebner Premier, Christine Kuehner, and Peter Kirsch. Increased involvement of the parahippocampal gyri in a sad mood predicts future depressive symptoms. *SCAN*, 9:2034–2040, February 2014.
75. Navkiran Kalsi, Daniela Altavilla, Renata Tambelli, Paola Aceto, Cristina Trentini, Chiara Di Giorgio, and Carlo Lai. Neural Correlates of Outcome of the Psychotherapy Compared to Antidepressant Therapy in Anxiety and Depression Disorders: A Meta-Analysis. *Frontiers in Psychology*, 8(927), June 2017.
76. Preeti Sinha, R. Venkateswara Reddy, Purna Srivastava, and Urvakhsh M. Mehta. Network neurobiology of electroconvulsive therapy in patients with depression. *Psychiatry Research: Neuroimaging*, 287:31–40, March 2019.
77. Zhexue Xu, Jing Zhang, Di Wang, Ting Wang, Shu Zhang, Xi Ren, Xiaolei Zhu, Atsushi Kamiya, Jiliang Fang, and Miao Qu. Altered Brain Function in Drug-Naïve Major Depressive Disorder Patients With Early-Life Maltreatment: A Resting-State fMRI Study. *Frontiers in Psychiatry*, 10(255), April 2019.
78. Sophie R. DelDonno, Lisanne M. Jenkins, Natania A. Crane, Robin Nusslock, Kelly A. Ryan, Stewart A. Shankman, Luan Phan, and Scott A. Langenecker. Affective Traits and History of Depression Are Related to Ventral Striatum Connectivity. *J Affect Disord.*, 221:72–80, October 2018.

79. Xiaoyue Ma, Jia Liu, Taiyuan Liu, Lun Ma, Wenhui Wang, Shaojie Shi, Yan Wang, Qiyong Gong, and Meiyun Wang. Altered Resting-State Functional Activity in Medication-Naive Patients With First-Episode Major Depression Disorder vs. Healthy Control: A Quantitative Meta-Analysis. *Frontiers in Behavioral Neuroscience*, 13(89), May 2019.
80. Changjun Teng, Jing Zhou, Hui Ma, Yarong Tan, Xin Wu, Chengbin Guan, Huifen Qiao, Jijun Li, Yuan Zhong, Chun Wang, and Ning Zhang. Abnormal resting state activity of left middle occipital gyrus and its functional connectivity in female patients with major depressive disorder. *BMC Psychiatry*, 18(370), 2018.
81. Fei-Fei Zhang, Wei Peng, John A. Sweeney, Zhi-Yun Jia, and Qi-Yong Gong. Brain structure alterations in depression: Psychoradiological evidence. *CNS Neuroscience & Therapeutics*, 24:994–1003, February 2017.
82. Ziqi Chen, Huawei Zhang, Zhiyun Jia, Jingjie Zhang, Xiaoqi Huang, Mingying Du, Lizhou Chen, Weihong Kuang, John A. Sweeney, and Qiyong Gong. Magnetization Transfer Imaging of Suicidal Patients with Major Depressive Disorder. *Scientific Reports*, 5(9670), April 2015.
83. Fradkin Y, Khadka S, Bessette KL, and Stevens MC. The relationship of impulsivity and cortical thickness in depressed and non-depressed adolescents. *Brain Imaging Behav*, 11(5):1515–1525, October 2017.
84. Tomoki Tokuda, Junichiro Yoshimoto, Yu Shimizu, Go Okada, Masahiro Takamura, Yasumasa Okamoto, Shigeto Yamawaki, and Kenji Doya. Identification of depression subtypes and relevant brain regions using a data-driven approach. *Scientific Reports*, 8(14082), September 2018.
85. Jun-Cheng Weng, Yu-Syuan Chou, Yuan-Hsiung Tsai, Chun-Te Lee, Ming-Hong Hsieh, and Vincent Chin-Hung Chen. Connectome Analysis of Brain Functional Network Alterations in Depressive Patients with Suicidal Attempt. *Journal of Clinical Medicine*, 8(1966), November 2019.
86. Gaizhi Li, Kathryn Rossbach, Aixia Zhang, Penghong Liu, and Kerang Zhang. Resting-state functional changes in the precuneus within first-episode drug-naive patients with MDD. *Neuropsychiatric Disease and Treatment*, 14:1991–1998, 2018.
87. Zi-Qi Chen, Ming-Ying Du, You-Jin Zhao, Xiao-Qi Huang, Jing Li, Su Lui, Jun-Mei Hu, Huai-Qiang Sun, Jia Liu, Graham J. Kemp, and Qi-Yong Gong. Voxel-wise meta-analyses of brain blood flow and local synchrony abnormalities in medication-free patients with major depressive disorder. *J Psychiatry Neurosci*, 40(6), April 2015.
88. Osamu Abe, Hidenori Yamasue, Kiyoto Kasai, Haruyasu Yamada, Shigeki Aoki, Hideyuki Inoue, Kunio Takei, Motomu Suga, Koji Matsuo, Tadafumi Kato, Yoshitaka Masutani, and Kuni Ohtomo. Voxel-based analyses of gray/white matter volume and diffusion tensor data in major depression. *Psychiatry Research: Neuroimaging*, 181:64–70, July 2010.
89. Tomislav D. Zbozinek, Raphael D. Rose, Kate B. Wolitzky Taylor, Cathy Sherbourne, Greer Sullivan, Murray B. Stein, Peter P. Roy Byrne, and Michelle G. Craske. Diagnostic Overlap of Generalized Anxiety Disorder and Major Depressive Disorder in a Primary Care Sample. *Depress Anxiety*, 29(12):1065–1071, December 2012.

90. Robert M. A. Hirschfeld. The Comorbidity of Major Depression and Anxiety Dis- 713
orders: Recognition and Management in Primary Care. *Primary Care Companion* 714
J Clin Psychiatry, 3(6):244–254, December 2001. 715
91. Yongjie Zhou, Zhongqiang Cao, Mei Yang, Xiaoyan Xi, Yiyang Guo, Maosheng 716
Fang, Lijuan Cheng, and Yukai Du. Comorbid generalized anxiety disorder and 717
its association with quality of life in patients with major depressive disorder. 718
Scientific Reports, 7(40511), January 2017. 719